Fatigue cracking in gamma titanium aluminide

Claire F. Trant[a], Trevor C. Lindley[a], Nigel Martin[b], Mark Dixon[b], David Dye[a]

[a]*Department of Materials, Royal School of Mines, Imperial College, Prince Consort Road, London, SW7 2BP, UK*
[b]*Rolls-Royce plc., PO Box 31, Derby, DE24 8BJ, UK*

Abstract

Fatigue crack initiation and growth were examined in cast and HIP'ed γ-TiAl 4522XD. It was found that fatigue crack growth rates were higher at 750°C than 400°C, but that ΔK_{th} was also higher. Temperature excursions between 400 and 750°C during fatigue crack growth resulted in retardation of the crack growth rate, both on heating and cooling; however heating from 400 to 750°C at a ΔK that would then be below threshold did not result in complete crack arrest. It was also found that for notches 0.6 mm in length and smaller, initiation from the microstructure could instead be observed at stresses similar to the material failure stress; a microstructural initiation site exists. Secondary cracking around borides could also be observed. A change from trans- to mixed trans-, inter- and intra-lamellar cracking could be observed where the estimated size of the crack tip plastic zone exceeded the colony size. Changes in fracture surface morphology could not be related to the temperature of fatigue crack growth, although this could be observed from the oxide scale colouration. Compressive pre-loading of a crack results in retardation of the crack, which could also be observed from the oxide.

Keywords: fatigue; intermetallics; electron microscopy

1. Introduction

γ-TiAl based alloys have long been attractive for use in jet engines due to their low density, around 4 g cm^{-3}, strength, oxidation resistance and creep resistance at intermediate temperatures in the range of 450–700°C [1]. In common with most intermetallics, this is because their ductility and toughness are quite limited, due to their large unit cells and hence dislocation Burgers vector lengths. This has prompted development efforts stretching back as far as 1953 [2], but only recently have this class of alloys begun to see service in civil jet engines [3]. Commercial alloys in this class largely use a two-phase structure consisting of a majority tetragonal $L1_0$ γ-TiAl phase with some hexagonal DO_{19} α_2-Ti_3Al phase. In cast microstructures the TiB_2 phase is used as a grain refiner of the prior-β grains [4], (β is the *bcc* high temperature solid solution phase of Ti), with a fully lamellar γ+α_2 microstructure obtained within these grains. Whilst these microstructures are not ductile at room temperature, they are found to be relatively tough, which enables their use in gas turbine components where some resistance to fatigue crack initiation is required, *e.g.* around features, foreign object damage or manufacturing imperfections. The two phase multilayer lamellar system within the grains shows improved mechanical properties when the lamellae are of a reduced thickness [5, 6]. Due to the tendency for interfaces to take a preference for the lowest interfacial energy, there is a common orientation relationship between the phases at the lamellar boundaries. The matching close packed planes and directions are $\{111\}_\gamma \parallel (0001)_{\alpha_2}$ and $<1\bar{1}0]_\gamma \parallel <11\bar{2}0>_{\alpha_2}$ [3]. Due to the symmetry of the γ phase there are six orientation variants. Due to these six rotation variants of the γ phase, the $\gamma \parallel \gamma$ boundaries can be pseudo twins with a 60° misorientation, 120° rotational faults or true twins with 180° rotation, from the highest to lowest interfacial energy variant respectively [7].

Overall ductility in both the α_2 phase and the γ phase independently increase with increasing temperature from room temperature (RT) up to 800°C [8], as well as the ductility of the overall alloy. Deformation at RT is mainly confined to the γ phase of the two phase alloy [9–15], deforming by octahedral glide of ordinary dislocations with the Burgers vector **b**=1/2<110] [16] and super dislocations with the Burgers vectors **b**=<101] and **b**=1/2 $<11\bar{2}]$ [17, 18]. Mechanical twinning in the γ is a secondary deformation mode [15]. α_2 is seen to deform less, attributed to its increased solubility for alloying elements compared to the γ phase. This is understood to happen because dislocations are more easily pinned, *e.g.* at solute atoms, and so its plasticity is more limited [3].

Deformation at 800°C is mainly transferred by the γ phase due to glide modes similar to those occurring at RT, with the addition of increased strain accommodation from climb of ordinary dislocations [19, 20], relaxing the need for independent slip systems. γ also has increased mechanical twinning at higher temperatures. Increasing temperature increases the activation of prismatic, basal and pyramidal slip in α_2, with ease of activation in that order [21]. Pyramidal slip can be seen to decrease at intermediate temperatures [3]. Due to pyramidal slip being the only glide plane to have a *c* component, it is required for general plasticity of the material. However, due to prismatic slip increasing at higher temperatures, and pyramidal slip decreasing at intermediate temperatures, this causes a strong preference for prismatic slip, and can contribute to a decrease in the ductility of the α_2 phase at increased temperatures [22–25]. The increase in number of available deformation mechanisms

in both phases reduces the occurrence of interfacial incompatibility between deformation in each of the the two phases and contributes to increased ductility at increased temperatures, due to improved slip transfer.

It remains the case, however, that the limited ductility and relatively fast crack propagation of γ-TiAl make its use as a material for highly stressed components particularly challenging. Fatigue crack growth threshold ΔK_{th} has been identified as a key material property for design, supported by an improved understanding of the deformation mechanisms associated with a crack growing near-threshold. For example, cracks can be seen to be locally arrested by a change in colony orientation [26]. Excursions in temperature may also be of interest, as the γ phase can activate additional deformation mechanisms at around 750 °C, rendering it ductile. Therefore in this paper, the effect of temperature excursions on the fatigue crack growth behaviour and associated fracture surface features are examined in a commercial γ-TiAl alloy, cast 4522XD (Ti-45Al-2Mn-2Nb-0.8 vol.% TiB_2-XD).

2. Experimental Procedures

The alloy composition is provided in Table 1. The as-cast and HIP'ed microstructure is shown in Figure 1(a). Within the prior-β grains randomly oriented $\gamma + \alpha_2$ colonies were found, 40-100 µm in size, consisting of 92% fraction of γ lamellae, 0.5 - 3.6 µm in plate width, averaging 1.4 µm, often with several plates together. The γ is interleaved with thin ligaments of α_2, 0.2 - 0.5 µm in plate width, averaging 0.3 µm [27].

Ti	Al	Mn	Nb	B	Si	O
bal.	43.90	1.80	1.90	0.90	0.20	0.14

Table 1: Composition of the 4522XD alloy studied, in at.%, measured by ICP-OES and LECO analysis. 2 vol.% TiB_2 was added to the melt, and the H content was found to be < 10 ppmw.

Cast bars were machined to form M12 threaded 5 × 5 mm square section specimens with gauge length 15 mm with a machined corner notch, 0.5 mm in depth. The specimen gauge lengths were then hand polished using OPS. Indirect crack growth measurement was carried out using the direct current potential drop (DCPD) technique. The loading waveform was sinusoidal, R=0.1, at a frequency of 5 Hz. Measuring fatigue crack growth of small cracks required 2 x 0.063 mm diameter probes spot welded either side of the specimen notch. The specimen was inserted and the load stabilised at 1 kN, the temperature was then increased and stabilised. Threshold was determined using incremental increases in ΔK until a crack growth rate of 10^{-10} m / cycle was observed over 10^4 cycles. For tests with a varied temperature, the crack growth was paused at a predetermined ΔK. The loading waveform was paused, load decreased to a nominal value and the temperature increased, stabilised within ±0.5% of the desired temperature, using a three-zone radiant furnace. The temperature was measured using a thermocouple located on the shoulder of the sample. The load was then returned to the mean value, and the loading waveform re-applied. The crack was then left to grow until a larger, pre-determined ΔK. The waveform was again paused, load decreased, and temperature returned to the original temperature, and left to stabilise. The same waveform was again re-applied and the crack allowed to grow until failure, Figure 13. Resulting fracture surfaces were then polished perpendicular through the face diagonal, again using OPS, in preparation for SEM and EBSD, Figure 1(b).

The relationship between the crack length and the potential drop must be determined via calibration. This requires creating features in the fracture surface at a known potential drops. γ-(TiAl) does not form striations when undergoing an overload, so calibration was carried out using heat tinting of the fracture

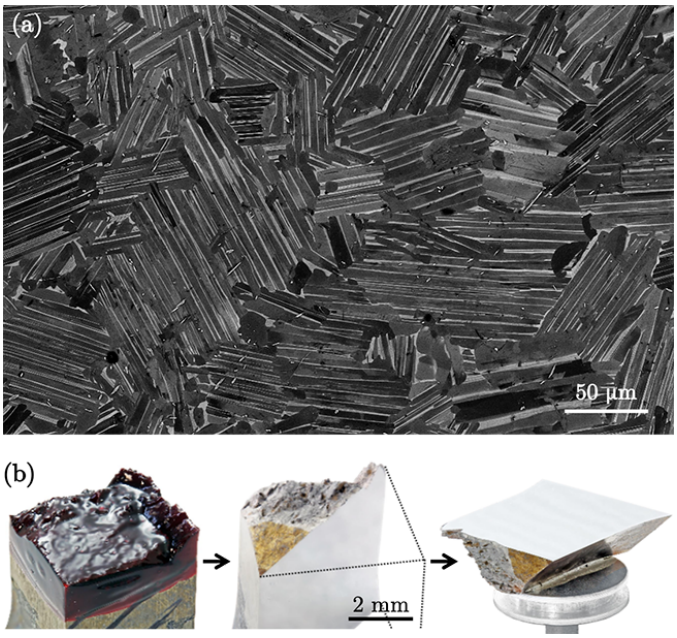

Figure 1: (a) Microstructure of as-cast, HIP'ed γ-TiAl. (b) Sectioning, polishing and mounting of the fractured specimen for SEM and EBSD. Images courtesy of Tom Zalewski, Rolls-Royce plc..

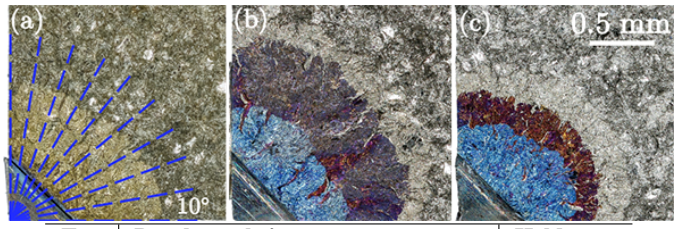

Test	Beach marks'	Held at
a 1	109 µV growth, 400°C for 260 mins	Mean load
b 1	60 µV growth, 650°C for 240 mins	Max load
2	170 µV growth, 550°C for 240 mins	Max load
3	70 µV growth, overload	Max load
c 1	78 µV growth, 650°C for 240 mins	Max load
2	79 µV growth, 550°C for 240 mins	Max load
3	80 µV growth, overload	Max load

Figure 2: The crack front was measured every 10° and averaged, overlaid on cropped fracture surface of (a) calibration a with only one data point. (b) Calibration b with three crack fronts, (c) calibration c with three crack fronts. Photography courtesy of Failure Investigation, Derby, Rolls-Royce plc.. The table of methods used to generate the features on the fracture surfaces.

surface. This was carried out at various time intervals in order to allow oxidation, leaving 'beach marks' of decreasing oxidation thickness, summarised in Figure 2. The specimen was then held at load so as to hold open the crack to allow oxidation. The crack length of each 'beach mark' was measured every 10° and an average taken of these values. Figure 2 gives seven 'beach marks' on three specimens, therefore seven points for the calibration curve. The datum point for zero potential drop can also be included, with the crack length of the starter notch. These give the calibration curve, Figure 3, with the data points labelled with their relative 'beach mark'. The calibration curve was created in accordance with [28]. The calculations for the change in stress intensity factor ΔK for the corner crack specimen used throughout can be found in [29].

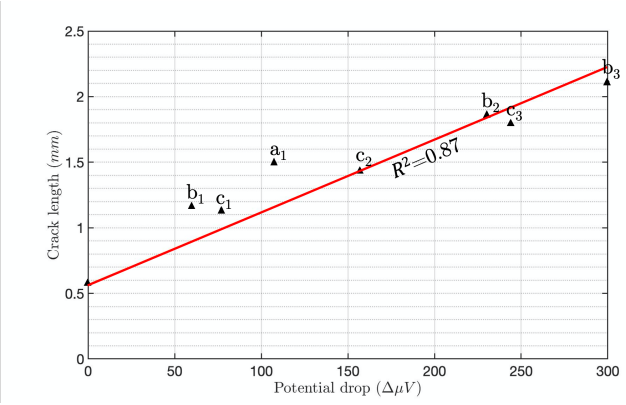

Figure 3: Data points from calibration samples and the zero datum point, to give the DCPD calibration used.

3. Results

3.1. Temperature Excursions

Isothermal response fatigue crack growth curves at 400 and 750°C are shown in Figure 4, with a guide to the eye in a solid line for the Paris region and a dotted line for the threshold. At 400°C ΔK_{th} in trans-lamellar fracture mode was 4.02 ± 0.12 MPa $\sqrt{\text{m}}$ from nine specimens. At an increased temperature of 750°C, trans-lamellar ΔK_{th} increases to 7.1 MPa $\sqrt{\text{m}}$. This was tested using 0.5 mm notched specimens, and therefore initiating through multiple randomly oriented colonies local to the notch and therefore in trans-lamellar fracture mode. The fatigue crack growth rates in the steady-state (Paris) fatigue crack growth regime are observed to be greater at 750°C than 400°C, with a concomitant reduction in life.

Four tests were carried out in which the temperature was increased from 400 to 750°C for differing ranges of ΔK, summarised in Figure 5. Each of the fatigue crack growth curves show blue data points at 400°C and red data points at 750°C. This data is overlain with a blue line for the isothermal response curve at 400°C and a red line for the isothermal response curve at 750°C, from Figure 4.

Test A, Figure 5(A), had an increase in temperature in the range from 7.8 MPa $\sqrt{\text{m}}$ to 9.4 MPa $\sqrt{\text{m}}$. In the increased temperature region there is seen to be an initial burst in growth, showing a high crack growth rate. This is thought to be due to the crack growing in inter-lamellar fracture mode through a colony. This high crack growth rate is short lived. The fracture path is impeded by the following colony. The ΔK is then close to the trans-lamellar fatigue crack growth threshold at 750°C in air, and therefore the crack growth rate slowly stabilises. It is uncertain whether it would eventually grow out to equilibrium for 750°C. When the temperature is then decreased again, the crack growth rate retards due to a larger plastic zone size and larger yield stress, 430 MPa at 400°C and 350 MPa at 750°C. This slowly grows out to equilibrium to the isothermal response curve for 400°C.

Test B, Figure 5(B), can be seen to give similar results, with the elevated temperature portion in the ΔK range from 7.0 MPa $\sqrt{\text{m}}$ to 11.1 MPa $\sqrt{\text{m}}$. In the increased temperature region, this test can be seen to show an initial burst of growth due to growing in inter-lamellar fracture mode, and then being impeded by the following colony. The crack growth rate grows out to equilibrium more slowly than test A due to the stress intensity factor range being closer to the trans-lamellar fracture mode threshold at 750°C in air. Test B again gives no indication that the crack growth rate would have grown out to the isothermal response curve at 750°C.

In test C, Figure 5(C), the increase to 750°C was performed below the isothermal fatigue crack growth threshold in trans-lamellar fracture mode at 750°C. The temperature was increased from 400 to 750°C at ΔK of 5.6 MPa $\sqrt{\text{m}}$, but trans-lamellar ΔK_{th} is 7.1 MPa $\sqrt{\text{m}}$ at 750°C. This caused the crack growth to retard by a multiple of 10^3. However, due to the sharp crack already initiated, the crack slowly grows out. This gives the fatigue crack growth threshold in inter-lamellar fracture mode at 750°C in air to be 5.8 MPa $\sqrt{\text{m}}$. It is again uncertain whether this increase in temperature region grows out to the 750°C fatigue crack growth curve. Once the temperature was decreased again at ΔK of 12 MPa $\sqrt{\text{m}}$ the bigger plastic

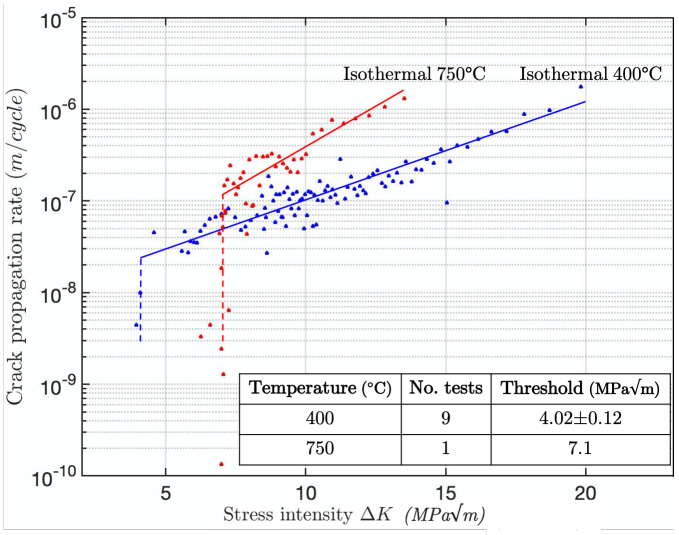

Figure 4: Isothermal fatigue crack growth curves obtained at 400 and 750°C in γ-(TiAl) alloy 4522XD in the as-cast and HIP condition. Guides to the eye are added to aid the reader.

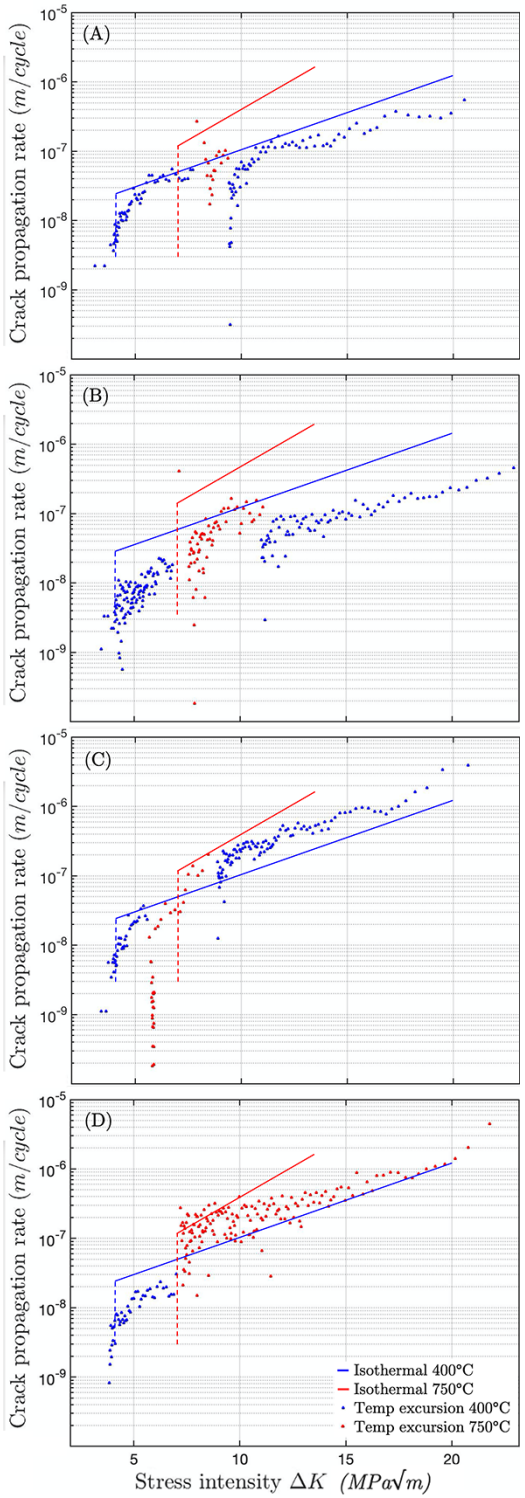

Test	ΔK temperature increase (MPa $\sqrt{m}$)	ΔK temperature decrease (MPa $\sqrt{m}$)
A	7.8	9.4
B	7.0	11.1
C	5.6	8.5
D	7.4	n/a

Figure 5: Fatigue crack growth tests, with a temperature increase from 400 to 750°C. The isothermal behaviour guides-to-the-eye are overlain.

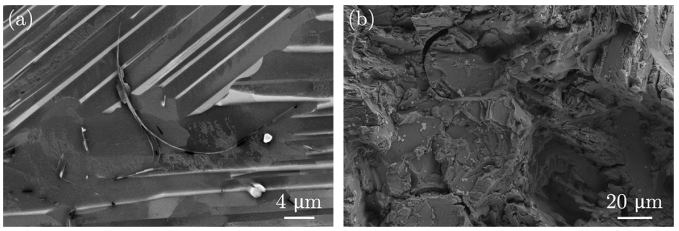

Figure 6: (a) Backscattered electron image of a wavy boride. (b) Secondary cracking on the fracture surface around a boride.

zone size again retards crack growth.

In test D, Figure 5(D), the temperature was increased to 750°C at a ΔK of 7.4 MPa $\sqrt{m}$ until failure, without returning to 400°C. There is large variability in the crack propagation rate for the same material in the same test environment. In Figures 5(A)–(D) it can be seen that when the temperature is increased from 400 to 750°C, whilst the isothermal response of Figure 4 is not recovered, the grown-out crack growth rate is always higher than at 400 °C, albeit with some variability due to the relatively coarse prior-β grain size.

Around a crack tip bifurcation of the crack may often take place, but as these link up to provide overall crack advance this may leave behind cracked ligaments that did not ultimately propagate. Furthermore, residual stresses and closure effects may also lead to cracking in the plastic wake. This can occur during any of the cracking modes, around grain boundaries, or through borides. The grain boundary borides were wavy in appearance, as shown in Figure 6(a), and are associated with such secondary cracking, as can be seen in Figure 6(b).

Figure 7 is an EBSD map perpendicular to fracture surface delineations. Figure 7(a) shows the phase map, green is the γ phase, blue is the α_2 phase. Within a single colony α_2 has a single orientation due to it originating from the same parent α. It can therefore be deduced that the region depicted is a single colony due to Figure 7(b) showing the orientation of the

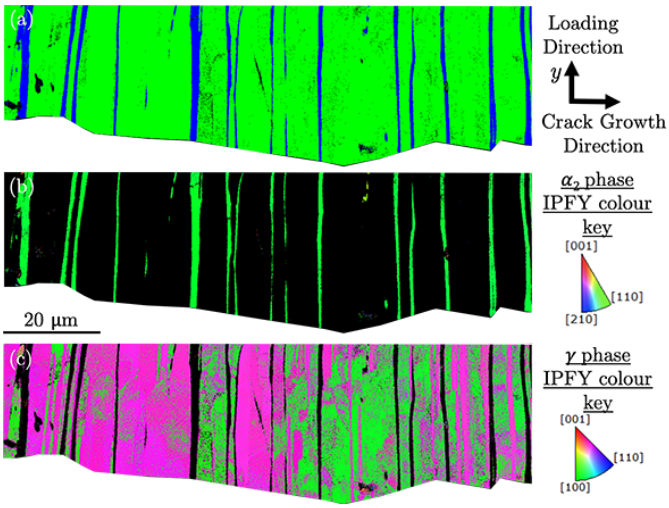

Figure 7: EBSD map of delineations where the loading direction and y direction are aligned. (a) Phase map of $_2$ and . (b) Orientation map of $_2$. (c) Orientation map of .

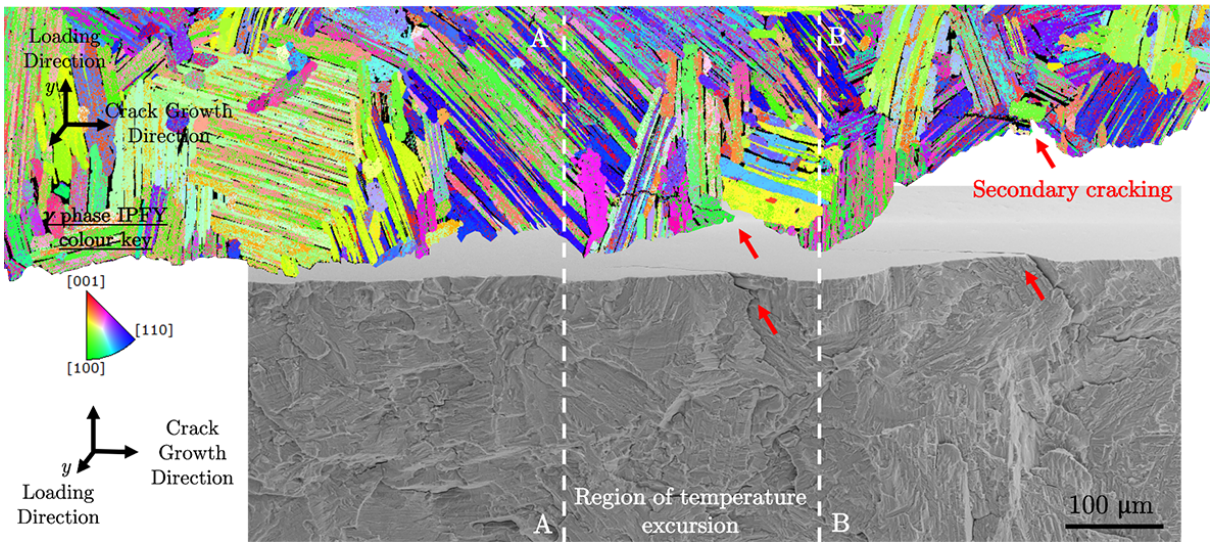

Figure 8: Temperature excursion test 1 EBSD map of the cross section perpendicular to the fracture surface through the region of temperature excursion, SEM image below directly relating to the EBSD. The loading direction and y direction are aligned up the page for the EBSD.

α_2 being the same throughout. Figure 7(c) shows just the γ phase. This shows two orientations of the phase. However, because γ–TiAl is only marginally tetragonal (2% difference between a and c), Hough transform-based EBSD using only the major Hough peaks can find it difficult to uniquely assign an orientation. This is manifest as the assignment of green and pink IPF colours to what are clearly the same colony of γ plates (which could be alternately twinned).

The fracture surface of test A was polished back perpendicular to the surface and an EBSD map (of the γ phase only) was generated of the region before, during and after the temperature excursion. This is shown in Figure 8 with an SEM image below of the corresponding perpendicular fracture surface. The SEM image shows no visible change in either morphology due to the increase in plastic zone size during the temperature excursion, or in contrast. The EBSD map shows no noticeable change through the temperature excursion with increased mechanical twinning or increased deformation. It can be seen that secondary cracking occurs in the reverse direction to the crack growth on the fracture surface. In this case, the secondary crack follows a grain boundary ahead, which may be related to stress relief in the plastic zone. In contrast, on inspection by light microscopy a marginally visible change in colouration could be observed due to, e.g. increased oxidation during the elevated temperature crack growth interval and the initial retardation of crack growth.

3.2. *Microstructural Initiation*

Threshold determination was performed by gradually increasing ΔK rather than by pre-cracking under the ΔK decreasing method because the specimens were rather short and the crack growth rates in the materials rather fast. The choice of specimen geometry was a consequence of matching the casting conditions closely to those that might be expected to be used in aerofoils, i.e. limited sample section size. However, this

Notch Size (mm)	**ΔK_{th}** (MPa $\sqrt{m}$)	**$\Delta\sigma$** (MPa)
0.03	n/a	540
0.06	n/a	393
0.1	4.0	331
0.1	4.1	340
0.25	4.0	209
0.5	4.02 ± 0.12	147 ± 5

Table 2: Measured effect of notch size on observed fatigue crack growth threshold at 450°C; average over nine samples for 0.5mm notches.

then gave rise to a concern about what, if any, effect plastic deformation associated with machining of the notch might have. Therefore the initial notch size was decreased to determine if there was any variation in the observed ΔK_{th}. Specimens with longer 0.1, 0.25 and 0.5 mm notches initiated from the notch through randomly oriented colonies, and show no effect from initial notch size on either trans-lamellar crack growth threshold or propagation, Table 2. Nine values of trans-lamellar ΔK_{th} were measured for 0.5 mm, two values for 0.1 mm and one value for 0.25 mm.

Specimens with shorter 0.06 and 0.03 mm notches initiated naturally, cracking from microstructural features away from the notch. The maximum stress at which the 0.06 mm specimen initiated from the microstructure was close to the 0.1% yield stress of 430 MPa (R=0.1), whilst in the 0.03 mm specimen the uniaxial yield stress was exceeded. Therefore it is inferred that the natural microstructural features available to initiate failure are both consistent with uniaxial testing and imply that surface machining artefacts smaller than 0.06 mm might be regarded as benign.

From the area of initiation, crack growth in fatigue was observed to be trans-lamellar, due to the plastic zone size being less than that of a colony, providing a flatter surface. With an increase in crack length, the stress intensity increases. Once

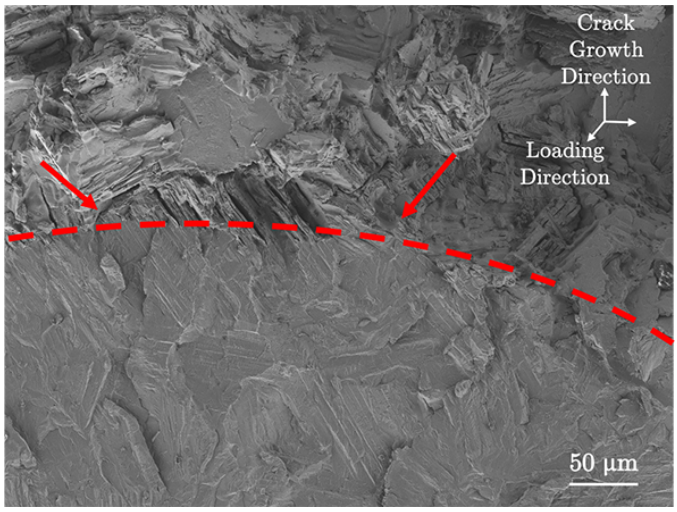

Figure 9: Change in plastic zone size to larger than that of a typical colony causes the cracking to transition from wholly trans-lamellar to mixed inter-, intra- and trans- lamellar. This causes the roughness to abruptly increase. This transition point is shown by the red arrows.

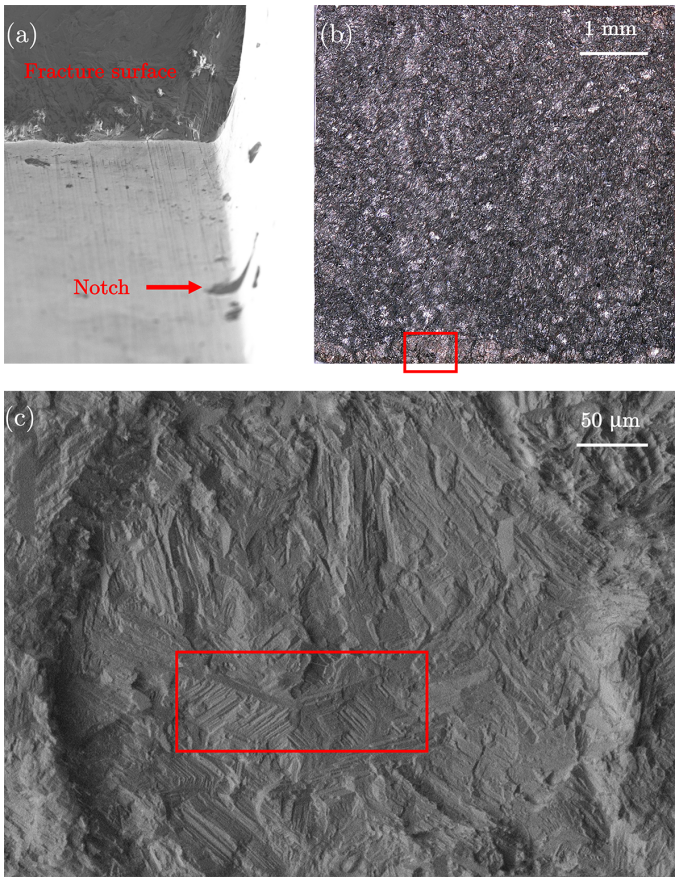

Figure 10: The 0.03 mm notched specimen initiated away from the notch. (a) The fracture surface can be seen at the top and the notch is indicated by the red arrow. (b) Fracture surface of the specimen with a small region of fatigue seen at the bottom of the micrograph, area of initiation marked by a red box. (c) Region of fatigue seen at the bottom of the fracture surface showing a near-circular, flatter region with trans-lamellar crack growth.

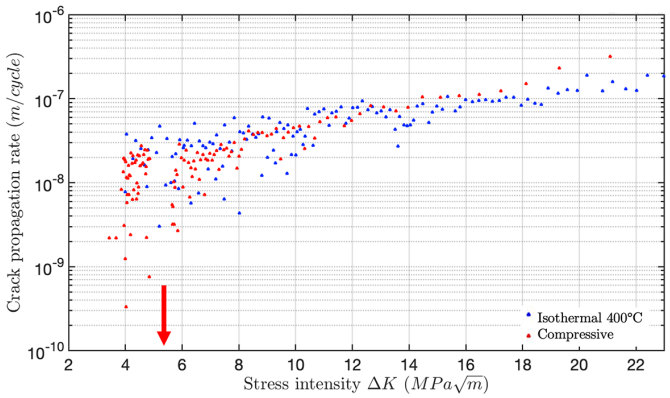

Figure 11: Fatigue crack growth curve of the application of the compressive load of 6 kN at a ΔK of approximately 5 MPa $\sqrt{\text{m}}$ indicated by the red arrow, compared to the isothermal response curve at 400°C.

this increased the plastic zone size to larger than the colony size, an increase in surface roughness could be observed, coinciding with a change in fracture mode to include inter- and intra-lamellar crack growth, Figure 9.

The specimen with the 0.03 mm FIB-machined notch initiated naturally from the central region of the gauge, but away from the notch which is indicated by the red arrows indicating the FIB-machined notch and fracture surface, Figure 10(a). A flatter region indicating fatigue could be observed at the bottom central side of the fracture surface which has been indicated by the red box in Figure 10(b). This region of fatigue, which exhibited a near-circular shape, can be seen in more detail in Figure 10(c). The roughness in this could be traced back to find an area of initiation. This initiation site is again observed to have a planar feature, with neighbouring intra-lamellar fracture, red box in Figure 10(c).

3.3. Effect of a compressive event

Application of a compressive load during crack growth causes crack retardation. Figure 11 shows the initial crack growth following that of the isothermal response curve at 400°C. At a ΔK of approximately 5 MPa $\sqrt{\text{m}}$ a compressive load of approximately 6 kN was applied (240 MPa). The crack growth rate could be seen to decrease, and then slowly grow out and return to the isothermal response curve. Figure 12 shows the fracture surface of this specimen. This fracture surface was tilted to expose the surface morphology. A region of interest has been selected, cropped and rotated. There is a brown ring that can be seen in early crack growth marked by the red arrows. This is due to the region being held at temperature for longer as the crack retarded and took longer to grow out after the compressive event. This shows that there is no indication on the fracture surface of this compressive loading being applied, e.g. in fracture morphology or roughness, other than the region of increased oxidation. SEM fractographic examination and white light interferometry also provided no evidence to allow the compressive event to be discerned on the fracture surface.

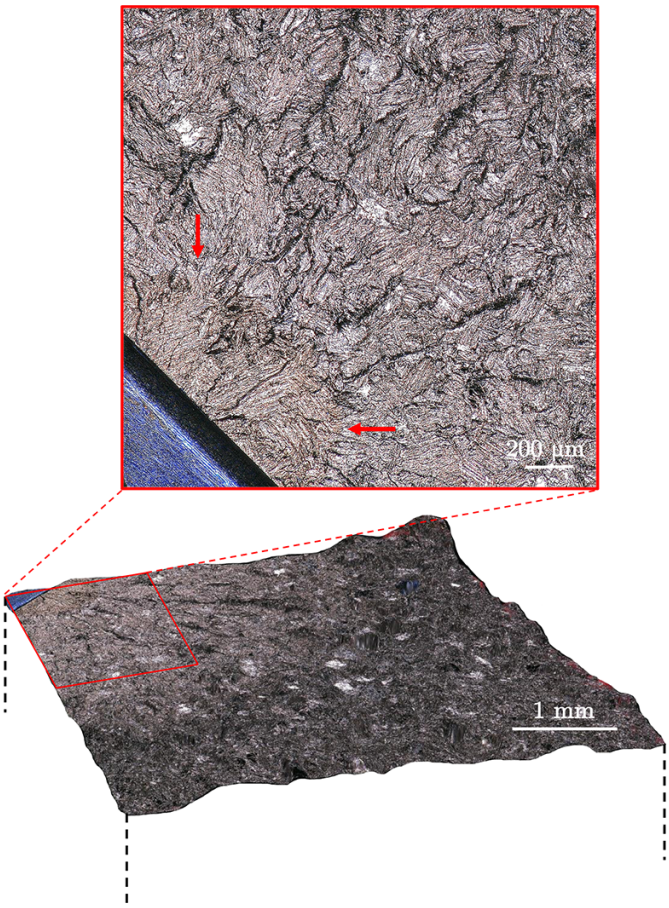

Figure 12: Tilted fracture surface of compressive load application during crack growth with cropped inlay. There is a brown ring in the early crack growth marked by red arrows. This is oxidation due to being held at temperature for longer than rest of sample when growing crack out after the application of the compressive load.

4. Conclusions

1) The fatigue crack growth threshold at 750°C in air for trans-lamellar fracture mode was found to be 7.1 MPa $\sqrt{\text{m}}$.

2) The fatigue crack growth threshold at 750°C in air for inter-lamellar fracture mode was found to be 5.8 MPa $\sqrt{\text{m}}$.

3) A step increase in temperature between the ΔK_{th} values for the inter-lamellar and trans-lamellar threshold values for the increased temperature causes an initial burst in the crack growth rate, quickly followed by a retardation in the crack growth rate. The crack growth rate is found to have greater retardation the closer the value of ΔK at which the temperature is increased at is to the inter-lamellar fracture mode ΔK_{th}.

4) A step decrease in temperature above the ΔK_{th} values shows crack growth rate retardation due to the larger plastic zone formed at the previously increased temperature.

5) The only method found in this work of detecting change in temperature is by optical microscopy, looking at the oxide scale colour. This oxide scale is not easily measurable, being less than a micron in thickness, in cross section. It not detectable by increased mechanical twinning in the region by looking at the EBSD maps obtained.

6) For specimens with a notch smaller than the size of a colony, ~70 µm, microstructural initiation was found to dominate.

7) Specimens with notches larger than the colony size initiated from the notch. Notch size was not found to have an effect on the fatigue crack growth threshold. The fatigue crack growth threshold for 0.5 mm starter notches was 4.02 ± 0.12 $MPa\sqrt{\text{m}}$ for nine specimens, 0.25 mm starter notch was 4.0 MPa $\sqrt{\text{m}}$ for one specimen, and 0.1 mm starter notches was 4.0 and 4.1 MPa $\sqrt{\text{m}}$ for two specimens. The fatigue crack growth threshold was therefore found to be 4.03 ± 0.11 $MPa\sqrt{\text{m}}$ for the twelve above listed specimens. These specimens initiated in trans-lamellar fracture mode from the randomly oriented colonies local to the notch.

8) Application of a compressive load during crack growth causes retardation in the crack growth.

Acknowledgements

This work was funded by EPSRC under a DTP CASE conversion, with specimens and additional funding provided by Rolls-Royce plc. The assistance of Dr Edward Saunders with the fractographic inspection and of Mr Jonathan Green with the macrophotography, both of Rolls-Royce plc., are gratefully acknowledged.

Data Availability

Data are available on request.

References

[1] H. Clemens, S. Mayer, Design, processing, microstructure, properties, and applications of advanced intermetallic TiAl alloys, Advanced Engineering Materials 15 (2013) 191–215.

[2] J. C. Williams, L. Gerd, Titanium, Springer-Verlag Berlin Heidelberg, New York (2003) 385.

[3] Fritz Appel, Jonathan David Heaton Paul, Michael Oehring, Gamma titanium aluminide alloys, Wiley-VCH, Weinheim (2011) 752.

[4] D. Larsen, L. Christodoulou, S. Kampe, R. Sadler, Investment-cast processing of XDTM near-gamma titanium aluminides, Materials Science and Engineering: A 144 (1991) 45 – 49.

[5] J. Kruzic, J. Campbell, A. McKelvey, H. Choe, R. Ritchie, Gamma titanium aluminides 1999, TMS, Warrendale, PA, (editors Y. W. Kim, D. M. Dimiduk and M. H. Loretto) (1999) 495.

[6] Y. Mine, K. Takashima, P. Bowen, Effect of lamellar spacing on fatigue crack growth behaviour of a TiAl-based aluminide with lamellar microstructure, Materials Science and Engineering: A 532 (2012) 13 – 20.

[7] F. Appel, R. Wagner, Microstructure and deformation of two-phase γ-titanium aluminides, Materials Science and Engineering R 22 (1998) 187 – 268.

[8] Y. W. Kim, Ordered intermetallic alloys, part III: gamma titanium aluminides, JOM 46 (1994) 30–39.

[9] J. B. Singh, G. Molénat, M. Sundararaman, S. Banerjee, G. Saada, P. Veyssière, A. Couret, The activation and the spreading of deformation in a fully lamellar Ti–47 at.% Al–1 at.% Cr–0.2 at.% Si alloy, Philosophical Magazine 86 (2006) 2429–2450.

[10] F. Appel, P. Beaven, R. Wagner, Deformation processes related to interfacial boundaries in two-phase γ-titanium aluminides, Acta Metallurgica et Materialia 41 (1993) 1721–1732.

[11] F. Appel, R. Wagner, Microstructure and deformation of two-phase γ-titanium aluminides, Materials Science and Engineering: R 22 (1998) 187–268.
[12] V. Vasudevan, M. Stucke, S. Court, H. Fraser, The influence of second phase Ti_3Al on the deformation mechanisms in TiAl, Philosophical Magazine Letters 59 (1989) 299–307.
[13] S. Sriram, D. M. Dimiduk, P. M. Hazzledine, V. K. Vasudevan, The geometry and nature of pinning points of 1/2<110] unit dislocations in binary TiAl alloys, Philosophical Magazine A 76 (1997) 965–993.
[14] J. Wiezorek, X. Zhang, A. Godfrey, D. Hu, M. Loretto, H. Fraser, Deformation behavior of α_2-lamellae in fully lamellar Ti-48Al-2Mn-2Nb at room temperature, Scripta Materialia 38 (1998) 811–817.
[15] J. Singh, G. Molénat, M. Sundararaman, S. Banerjee, G. Saada, P. Veyssière, A. Couret, In situ straining investigation of slip transfer across α_2 lamellae at room temperature in a lamellar TiAl alloy, Philosophical Magazine Letters 86 (2006) 47–60.
[16] D. Shechtman, M. J. Blackburn, H. A. Lipsitt, The plastic deformation of TiAl, Metallurgical Transactions 5 (1974) 1373–1381.
[17] H. A. Lipsitt, D. Shechtman, R. E. Schafrik, The deformation and fracture of TiAl at elevated temperatures, Metallurgical Transactions A 6 (1975) 1991–1996.
[18] G. Hug, A. Loiseau, A. Lasalmonie, Nature and dissociation of the dislocations in TiAl deformed at room temperature, Philosophical Magazine A 54 (1986) 47–65.
[19] B. K. Kad, H. L. Fraser, On the contribution of climb to high-temperature deformation in single phase γ-TiAl, Philosophical Magazine A 69 (1994) 689–699.
[20] M. Yoo, J. Morris, K. Ho, S. Agnew, Nonbasal deformation modes of HCP metals and alloys: role of dislocation source and mobility, Metallurgical and Materials Transactions A 33 (2002) 813–822.
[21] Y. Umakoshi, T. Nakano, T. Takenaka, K. Sumimoto, T. Yamane, Orientation and temperature dependence of yield stress and slip geometry of Ti_3Al and Ti_3Al-V single crystals, Acta Metallurgica et Materialia 41 (1993) 1149 – 1154.
[22] H. Inui, Y. Toda, M. Yamaguchi, Plastic deformation of single crystals of a $D0_{19}$ compound with an off-stoichiometric composition (Ti-36·5 at.% Al) at room temperature, Philosophical Magazine A 67 (1993) 1315–1332.
[23] Y. Minonishi, Dissociation of 1/3<1126 >{1121} superdislocations in Ti_3Al single crystals deformed at high temperatures, Materials Science and Engineering: A 192 (1995) 830–836.
[24] Y. Minonishi, Intermetallic compounds for high-temperature structural applications, in: SAMPE Symp. Proc., M. Yamaguchi and H. Fukutomi, eds., SAMPE, Chiba, Japan, pp. 1501–06 (1993).
[25] Y. Umakoshi, T. Nakano, K. Sumimoto, Y. Maeda, High-Temperature Ordered Intermatallics Alloys V, in: Mater. Res. Soc. Symp. Proc, volume 288, p. 441 (1993).
[26] M. S. Dahar, S. M. Seifi, B. P. Bewlay, J. J. Lewandowski, Effects of test orientation on fracture and fatigue crack growth behavior of third generation as-cast Ti-48Al-2Nb-2Cr, Intermetallics 57 (2015) 73–82.
[27] T. Edwards, F. D. Gioacchino, W. J. Clegg, N. Martin, M. Dixon, Plasticity of Titanium Aluminide, Presentation at H.J. Stone et al Eds, Beyond Nickel-Based Superalloys II, Cambridge, UK (2016).
[28] Test method for the determination of the rate of fatigue crack growth in metallic materials - corner crack geometry, Rolls-Royce technical report MMM310002 (2011).
[29] BSI, Aerospace series test methods for metallic materials. Determination of fatigue crack growth rates using corner-cracked (CC) test pieces. BSI Standard Publication - BS EN 3873:2010 (2010) 1–7.

Supplementary Information

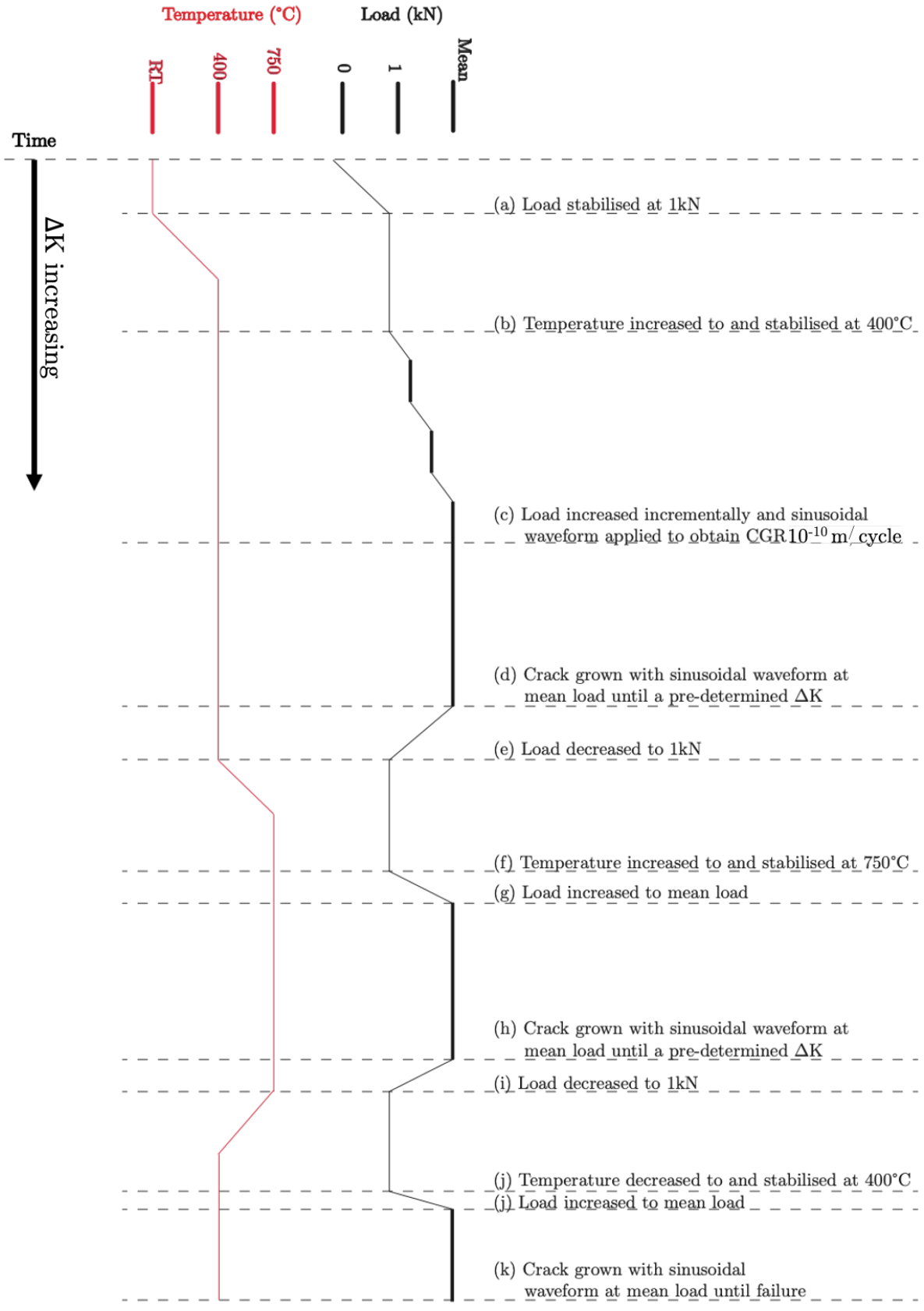

Figure 13: Evolution of temperature and maximum load during the fatigue testing through the test sequence, showing how the changes in temperature were applied.